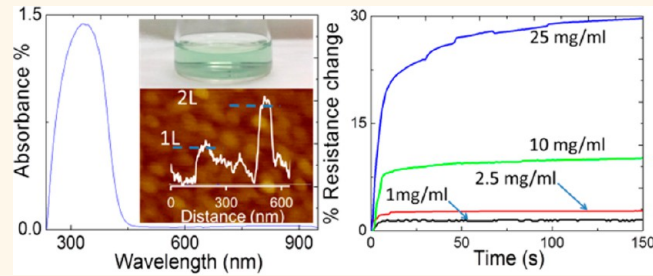


# Field Effect Biosensing Platform Based on 2D $\alpha$ -MoO<sub>3</sub>

Sivacarendran Balendhran,<sup>†,‡,§,\*</sup> Sumeet Walia,<sup>†,§</sup> Manal Alsaif,<sup>†</sup> Emily P. Nguyen,<sup>†</sup> Jian Zhen Ou,<sup>†</sup> Serge Zhuiykov,<sup>‡</sup> Sharath Sriram,<sup>†,§</sup> Madhu Bhaskaran,<sup>†,§</sup> and Kourosh Kalantar-zadeh<sup>†,\*</sup>

<sup>†</sup>School of Electrical and Computer Engineering, RMIT University, Melbourne, Victoria, Australia, <sup>‡</sup>Materials Science and Engineering Division, CSIRO, Highett, Victoria, Australia, and <sup>§</sup>Functional Materials and Microsystems Research Group, RMIT University, Melbourne, Victoria, Australia

**ABSTRACT** Electrical-based biosensing platforms offer ease of fabrication and simple sensing solutions. Recently, two-dimensional (2D) semiconductors have been proven to be excellent for the fabrication of field effect transistors (FETs) due to their large transconductance, which can be efficiently used for developing sensitive bioplatforms. We present a 2D molybdenum trioxide (MoO<sub>3</sub>) FET based biosensing platform, using bovine serum albumin as a model protein. The conduction channel is a nanostructured film made of 2D  $\alpha$ -MoO<sub>3</sub> nanoflakes, with the majority of nanoflake thicknesses being equal to or less than 2.8 nm. The response time is impressively low (less than 10 s), which is due to the high permittivity of the 2D  $\alpha$ -MoO<sub>3</sub> nanoflakes. The system offers a competitive solution for future biosensing applications.



**KEYWORDS:** two-dimensional materials · MoO<sub>3</sub> · bovine serum albumin · biosensing · exfoliation

In recent years, research on two-dimensional (2D) semiconductors has intensified significantly. These materials offer enhanced properties such as increased carrier mobility and tunability of band structures as well as enhanced thermal and mechanical properties.<sup>1–4</sup> Such desirable aspects are achieved through the quantum effects, which are imposed at atomically thin dimensions.<sup>1</sup> Although these 2D semiconductors have so far been increasingly studied for their various physical and chemical applications,<sup>5–10</sup> their biosensing capabilities are yet to be fully explored. More recently 2D molybdenum disulfide (MoS<sub>2</sub>)-based sensing of biomolecules has been reported, where the high fluorescence quenching efficiency of monolayered MoS<sub>2</sub> and different affinities toward single- and double-strand DNA have been utilized in sensing processes.<sup>11</sup> MoS<sub>2</sub>–graphene composites have also been used in electrochemical sensing, which can be potentially adopted for biosensing applications.<sup>12</sup>

A semiconductor that is naturally found in layered form and can be exfoliated into highly crystalline 2D planes is molybdenum trioxide (MoO<sub>3</sub>). MoO<sub>3</sub> has been proven applicable in an extensive range of electronic, optical, electrochromic, and sensing

applications.<sup>1,13–16</sup> For research in the 2D realm, the thermally stable polymorph  $\alpha$ -MoO<sub>3</sub> is of specific interest, as it exists in a layered form that can be resolved and exfoliated into atomically thin planes.  $\alpha$ -MoO<sub>3</sub> is composed of double layers of edge-sharing MoO<sub>6</sub> octahedra, vertically held together by weak van der Waals forces (Figure 1).<sup>17,18</sup>

Quite recently,  $\alpha$ -MoO<sub>3</sub> has emerged as an excellent 2D semiconductor for developing field effect transistors (FETs) with enhanced carrier mobilities, due to its favorable aspects such as high dielectric value and easily tunable band structure.<sup>17</sup> 2D MoO<sub>3</sub> layers have also been widely used as charge generation/injection layers in organic light emitting diodes (LEDs) and photovoltaic devices.<sup>19–23</sup>

Achieving 2D layers of MoO<sub>3</sub> via various types of top down exfoliation and bottom up synthesis methods has recently been demonstrated.<sup>18,24</sup> The mechanical exfoliation process has been shown to produce MoO<sub>3</sub> sheets as thin as 1.4 nm composed of a double layer.<sup>18</sup> Such a mechanical exfoliation technique results in highly pure and crystalline 2D sheets. However, it has a low yield. High-yield probe sonication and lithium ion (Li<sup>+</sup>)-based liquid exfoliation techniques have been proven to produce

\* Address correspondence to kourosh.kalantar@rmit.edu.au, shiva.balendhran@rmit.edu.au.

Received for review June 25, 2013 and accepted November 1, 2013.

Published online November 01, 2013  
10.1021/nn403241f

© 2013 American Chemical Society

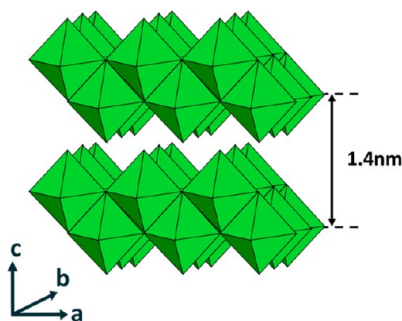


Figure 1.  $\alpha$ - $\text{MoO}_3$  crystal structure composed of edge-sharing double layers of  $\text{MoO}_6$  octahedra.

few-layered  $\text{MoO}_3$  nanosheets.<sup>24</sup> Furthermore, the oxidation of few-layered  $\text{MoS}_2$  flakes has also been employed in synthesizing 2D  $\text{MoO}_3$ .<sup>24</sup> Nevertheless, the effect of impurities and hydration during such processes should always be addressed. All the aforementioned aspects of 2D  $\text{MoO}_3$  inspire further exploration of its invaluable properties.

According to the Born approximation equation, several parameters increase the charge carrier scattering and as a result reduce electron mobility.<sup>25</sup> This includes acoustic and optical phonon scattering, Coulomb charges, and surface roughness.<sup>17,25</sup> The change in the carrier mobility alters the transconductance of the FET platform, and as such, this change can be associated with environmental stimuli that are targeted. Especially in biosensing applications, the effect of Coulombic charges can efficiently be used for influencing the field effect parameters of the 2D platforms. Many of the biomaterials, such as proteins, are intrinsically charged. Many other biosensing processes are associated with redox interactions that involve ionic charges. Additionally, the polar nature of the  $\text{MoO}_3$  surface facilitates the affinity and eventual adhesion of the Coulomb charges (the formation of electrical double layer for ionic charges and immobilization of organic entities such as proteins) onto its surface. 2D  $\text{MoO}_3$  can potentially be a great platform for the formation of FET-based chemical and biosensors. FETs based on 2D  $\text{MoO}_3$  structures with charge carrier mobilities exceeding  $1100 \text{ cm}^2 \text{ V}^{-1} \text{ s}^{-1}$  have been realized.<sup>17</sup> These values exceed mobilities of many of those of doped silicon and other 2D FETs.<sup>7,17,26</sup> Such enhanced mobilities and high sensitivity to Coulombic charges, due to their 2D morphology, allow 2D  $\text{MoO}_3$ -based FETs to be potentially used as transducing platforms for developing sensors with high sensitivities. Such aspects provide extensive opportunities for developing both charge- and electrochemical-based biosensors with enhanced performance, potentially competing against the current state of the art 1D and 0D biosensors.<sup>27,28</sup> As  $\alpha$ - $\text{MoO}_3$  is a wide-band-gap material ( $\sim 3.3 \text{ eV}$ ),<sup>17,29</sup> the threshold voltage ( $V_{\text{th}}$ ) to turn on the conduction channel would be relatively high. However, simple processes that offer band-gap

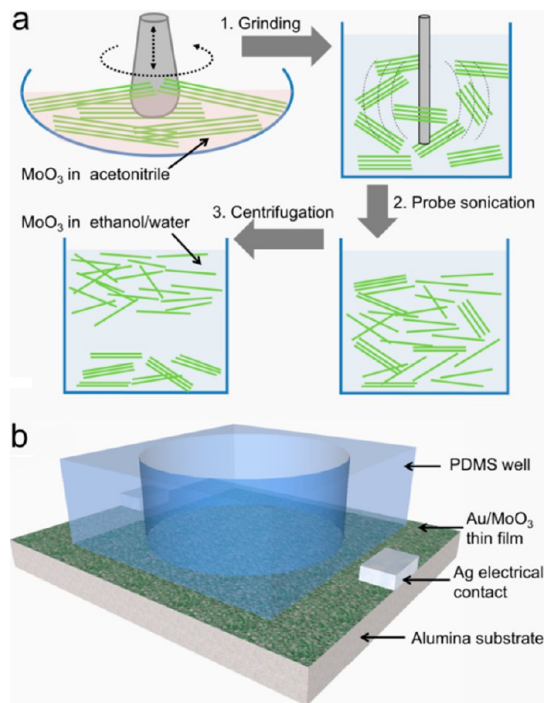


Figure 2. (a) Three-step liquid exfoliation process. Green lines denote atomically thin  $\alpha$ - $\text{MoO}_3$  nanosheets. (b) Three-dimensional schematic illustration of the fabricated sensor (not to scale).

tuning, such as embedding of Coulombic charges via ion intercalation, placing metallic catalysts on the surface of the material, and partial reduction of the compound, have all been proven to be effective in reducing the band gap.<sup>1,17,30</sup>

In this work, we explore the viability of a 2D  $\alpha$ - $\text{MoO}_3$ -based field effect biosensing platform and study the effect of Coulombic charges on this 2D transducing platform. Bovine serum albumin (BSA) is used as a model protein for this purpose. We propose a high-yield liquid exfoliation method for realizing nanostructured thin films made of 2D  $\text{MoO}_3$  flakes and, based on such films, present successful sensing of BSA at various concentrations.

## RESULTS AND DISCUSSION

A three-step liquid exfoliation process was established, based on previously reported literature, in order to obtain 2D  $\alpha$ - $\text{MoO}_3$  nanoflakes.<sup>31–34</sup> Figure 2a schematically demonstrates the process of obtaining the nanoflake suspension, and Figure 2b shows the three-dimensional (3D) schematic illustration of the sensors fabricated from the 2D  $\alpha$ - $\text{MoO}_3$  nanoflakes. The details are presented in the Experimental Section.

The UV-vis absorbance spectrum of the exfoliated  $\text{MoO}_3$  nanoflake suspension (Figure 3) shows an increase in absorbance in the range 350 to 450 nm. The suspension appears to be blue/yellow in color (Figure 3 inset), which is in agreement with the absorbance spectrum.

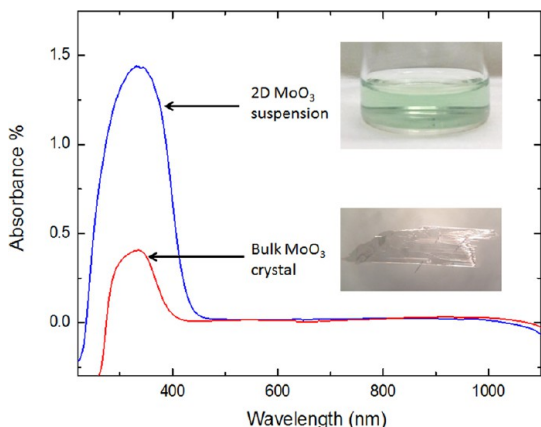


**Figure 3.** UV-vis range absorbance spectra of the exfoliated  $\alpha$ -MoO<sub>3</sub> suspension and bulk  $\alpha$ -MoO<sub>3</sub> crystal with inset showing their corresponding optical image.

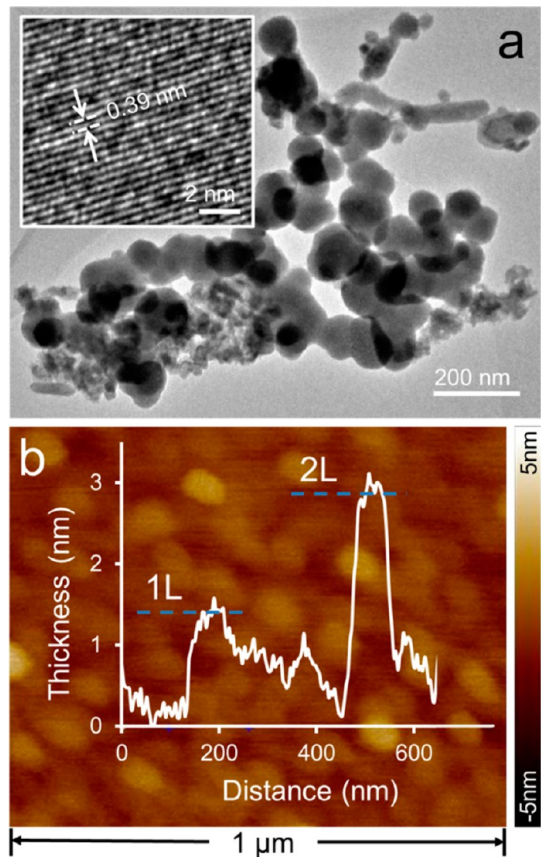


**Figure 4.** (a) TEM image of the 2D MoO<sub>3</sub> nanoflakes, with inset showing a magnified HRTEM image, clearly indicating the lattice spacing of  $\alpha$ -MoO<sub>3</sub>. (b) AFM scan of the MoO<sub>3</sub> nanoflakes with their cross sectional thickness profile (x-axis to scale) indicating the presence of double-layered and multiples of double-layer MoO<sub>3</sub> sheets ( $L \sim 1.4$  nm for a double layer).

Transmission electron microscopy (TEM) and atomic force microscopy (AFM) analyses were conducted in order to determine the crystal arrangement and 2D nature of the  $\alpha$ -MoO<sub>3</sub> nanoflakes from the suspension. TEM images (Figure 4a) reveal that the majority of

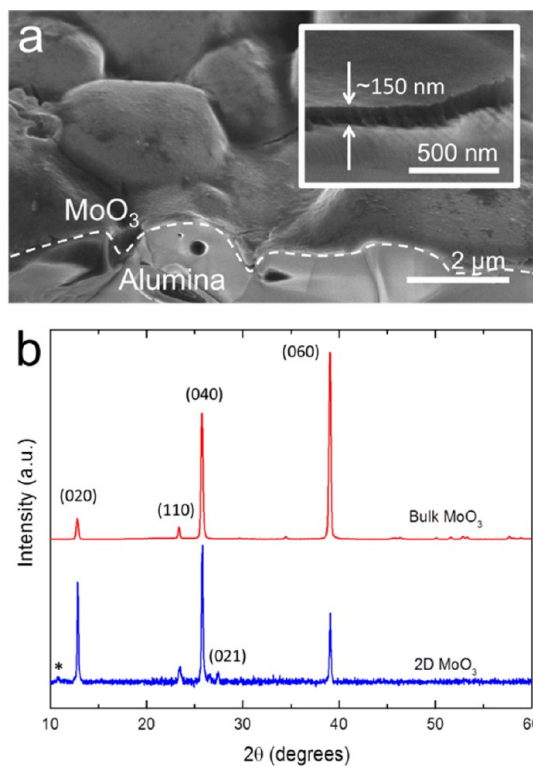


**Figure 5.** (a) Cross sectional SEM images of a nanostructured thin film made of 2D MoO<sub>3</sub> nanoflakes on an alumina substrate with inset showing the thickness of the film. (b) XRD patterns of a bulk MoO<sub>3</sub> crystal and a drop-casted nanostructured 2D MoO<sub>3</sub> thin film indicating the dominant presence of the layered  $\alpha$ -MoO<sub>3</sub> phase. Peaks corresponding to hydrated MoO<sub>3</sub> are denoted by [\*].

suspended particles are 2D  $\alpha$ -MoO<sub>3</sub> flakes with typical lateral dimensions in the range 50 to 150 nm. Some nanorod features are also occasionally seen. The high-resolution TEM (HRTEM) image (Figure 4a inset) clearly shows the typical lattice spacing of highly ordered  $\alpha$ -MoO<sub>3</sub> crystals as previously reported.<sup>17,18</sup> The lattice spacing of 0.39 nm is observed as evidence for a perfectly crystalline  $\alpha$ -MoO<sub>3</sub> planar structure.

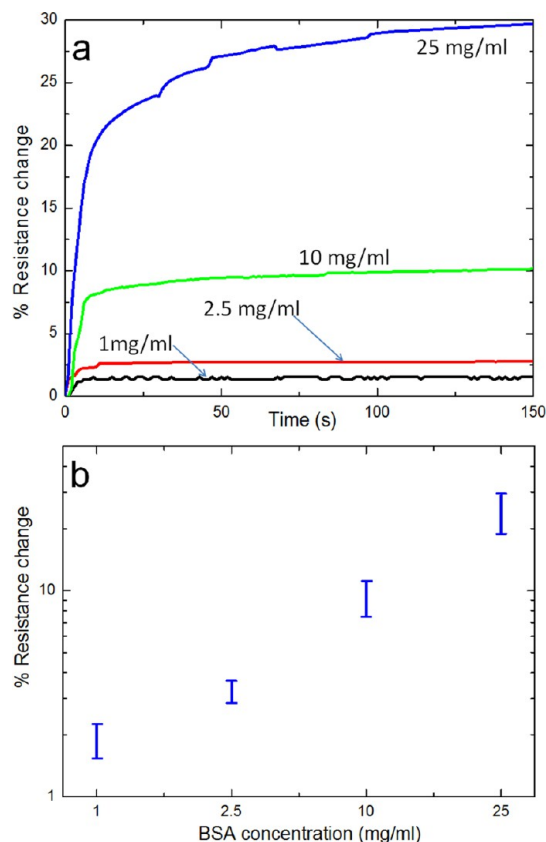
AFM analysis (Figure 4b) of the MoO<sub>3</sub> nanoflakes indicates the presence of single and few layers. The thickness profiles indicate that the flakes mostly exist in multiples of 1.4 nm, which corresponds to the thickness of a fundamental double-layered orthorhombic  $\alpha$ -MoO<sub>3</sub> nanosheet.<sup>17,18</sup> This is generally expected and commonly observed, since the double layers are composed of strong, covalently bonded MoO<sub>6</sub> octahedra.<sup>17,18</sup> The typical lateral dimensions observed in the AFM scans are also in agreement with the TEM results. The majority of the flakes were made of one double layer (1.4 nm) or two double layers (2.8 nm).

Figure 5a shows the cross sectional scanning electron microscope (SEM) image of a drop-casted MoO<sub>3</sub> thin film on a rough alumina substrate of micrometer size profile, annealed at 220 °C. The rough alumina substrate was chosen, as this superstate allows the formation of a homogeneous nanostructured MoO<sub>3</sub>

film after the drop casting. In contrast, homogeneous films were not obtained onto optically smooth silicon, glass, and quartz substrates. A compact layer of  $\text{MoO}_3$  was observed to have adopted the surface profile of the alumina substrate. As seen in the Figure 5a inset, the typical thickness of the film was approximately between 150 and 170 nm. The X-ray diffraction (XRD) analysis of the drop-casted and annealed thin film shows dominant peaks of layered orthorhombic  $\alpha\text{-MoO}_3$  and minor contributions of hydrated  $\text{MoO}_3$  (Figure 5b). The dominant peaks observed at  $12.8^\circ$ ,  $25.8^\circ$ , and  $39^\circ$  correspond to (020), (040), and (060) planes of  $\alpha\text{-MoO}_3$  (ICDD Card No. 35-0609), respectively.<sup>18,35</sup> This is indicative of the thin film composition that is largely composed of layered  $\alpha\text{-MoO}_3$  nanoflakes, which is also in agreement with the TEM analysis. In comparison to the bulk crystal, the (060) peak intensity was observed to have decreased for the nanostructured thin film made of 2D flakes. As the thin film is composed of 2D  $\text{MoO}_3$  nanoflakes, which are exfoliated at the van der Waals point of contact between planes, such a reduction in the peak intensity is expected.

As suggested in the introduction, BSA is used as a model protein for the sensing experiments presented in this paper. BSA sensing has been undertaken using different optical systems based on transmission/absorbance spectroscopy, surface-enhanced Raman spectroscopy (SERS), fluorescence spectroscopy, and resonance light scattering.<sup>36–39</sup> BSA has also been used for assessing electrochemical sensing platforms.<sup>40,41</sup>

FET-based sensors, made of nanostructured 2D  $\alpha\text{-MoO}_3$  thin films, were fabricated, and liquid wells, for applying the biosamples, were incorporated. Details of the fabrication of the sensors are presented in the Experimental Section. Prior to the BSA (Invitrogen) biosensing measurements, 15  $\mu\text{L}$  of Milli-Q water was poured into the polydimethylsiloxane (PDMS) well using a micropipet, and we waited  $\sim 3$  to 5 min to achieve a stable baseline. This was followed by the addition of 15  $\mu\text{L}$  of solution containing different concentrations of BSA in Milli-Q water using a micropipet into the already existing 15  $\mu\text{L}$  of Milli-Q in the well. The total 30  $\mu\text{L}$  solution was stirred for  $\sim 5$  s to allow the BSA solution to completely mix, resulting in the concentration of the BSA in the well to become half that of the added solution. After this, 15  $\mu\text{L}$  of the solution was extracted from the well in order to maintain the solution volume at a constant value to eliminate any effect of volumetric change in the dynamic response. The baseline was then adjusted to zero in order to remove any possible effect due to the pH change. Approximately 15 devices were fabricated, and each device was used for only a single sensing measurement. For these devices, the resistance of the active channels was in the range 10 to 60  $\text{k}\Omega$ .



**Figure 6.** (a) Dynamic response of the sensor as percentage resistance change at different concentrations of BSA (concentrations of 1, 2.5, 10, and 25  $\text{mg mL}^{-1}$ ). (b) Sensitivity graph: percentage resistance change vs concentration.

Electrical measurements were carried out to assess the effect of BSA immobilization onto the active surface of the  $\alpha\text{-MoO}_3$  FETs. The dynamic responses of the sensors, which were acquired at room temperature at different concentrations of BSA, are shown in Figure 6a. It was observed that the  $\text{MoO}_3$  film resistance increased on average by  $\sim 1.0\%$  for BSA concentrations as low as 1  $\text{mg mL}^{-1}$  ( $\sim 15 \mu\text{M}$ ). The average percentage change in resistance values of  $\sim 24.5\%$  was observed for maximum BSA concentrations of 25  $\text{mg mL}^{-1}$ . The response times were observed to be less than 10 s for all BSA concentrations. Measurements at each concentration were repeated on three devices to assess the repeatability of the sensors. Figure 6b shows the variation in the percentage resistance change as a function of the BSA concentration. The detection limit was obtained using the standard deviations in the signal/noise fluctuation, which was  $\sim 0.23\%$ , equal to 250  $\mu\text{g mL}^{-1}$ .

Raman spectroscopy was employed to investigate the immobilization of BSA onto nanostructured films made of 2D  $\text{MoO}_3$  nanoflakes. Figure 7 shows the Raman spectra acquired only on BSA and  $\text{MoO}_3$  as well as BSA (25  $\text{mg mL}^{-1}$ ) immobilized onto  $\text{MoO}_3$  ( $\text{BSA/MoO}_3$ ). Sharp peaks at 820 and 996  $\text{cm}^{-1}$  corresponding to the dominant M–O stretching modes as well as other vibrational modes are observed in the

$\text{MoO}_3$  spectrum.<sup>18,42</sup> The broad peak appearing at  $840\text{ cm}^{-1}$  and the broadening of the  $666\text{ cm}^{-1}$  peak indicate the presence of hydrated  $\text{MoO}_3$ ,<sup>30</sup> which is in agreement with the XRD analysis. The BSA spectrum shows distinct peaks at  $2925$  and  $2872\text{ cm}^{-1}$  as well as broad, low-intensity, organic peaks in the range

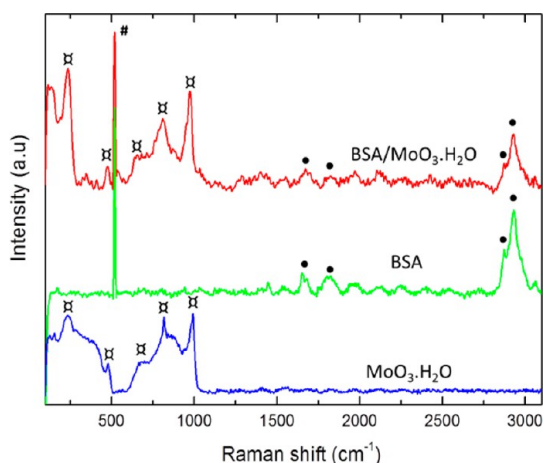


Figure 7. Normalized Raman spectra of drop-casted  $\text{MoO}_3$  thin film, BSA, and  $\text{BSA}/\text{MoO}_3$  on unpolished silicon substrates. Peaks denoted by (○)  $\text{MoO}_3$ , (●) BSA, and (#) Si.

$1600$ – $1850\text{ cm}^{-1}$ . The spectrum obtained on BSA/ $\text{MoO}_3$  displays clearly distinguished peaks of hydrated  $\text{MoO}_3$  as well as BSA, without any notable changes to the bond vibrational frequencies. The loss of sharpness and intensity in the dominant  $\text{MoO}_3$  peaks can be attributed to further hydration of the active  $\text{MoO}_3$  surface during the baselining and immobilization process. These results also suggest that the BSA has not covalently bonded to the  $\text{MoO}_3$  surface and that the immobilization has been achieved *via* collective van der Waals forces and electrostatic interactions, as also suggested previously.<sup>43,44</sup>

AFM was used for studying the surface roughness and the surface adhesion of both  $\text{MoO}_3$  and  $\text{BSA}/\text{MoO}_3$  surfaces. Figure 8a and b show the AFM roughness comparison between the  $\text{MoO}_3$  thin film and  $\text{BSA}/\text{MoO}_3$  surfaces. The average surface roughness value for  $\text{MoO}_3$  was observed to be  $45.3\text{ nm}$ , whereas for the  $\text{BSA}/\text{MoO}_3$  surface it was  $0.4\text{ nm}$  and became very smooth. This suggests that the BSA is densely immobilized onto the  $\text{MoO}_3$  surface and also fills the gaps.

Surface adhesive force mapping was conducted to assess the adhesion property of the surfaces. The voltage scale bars on Figure 8c and d directly correspond to the adhesive force between the AFM tip and

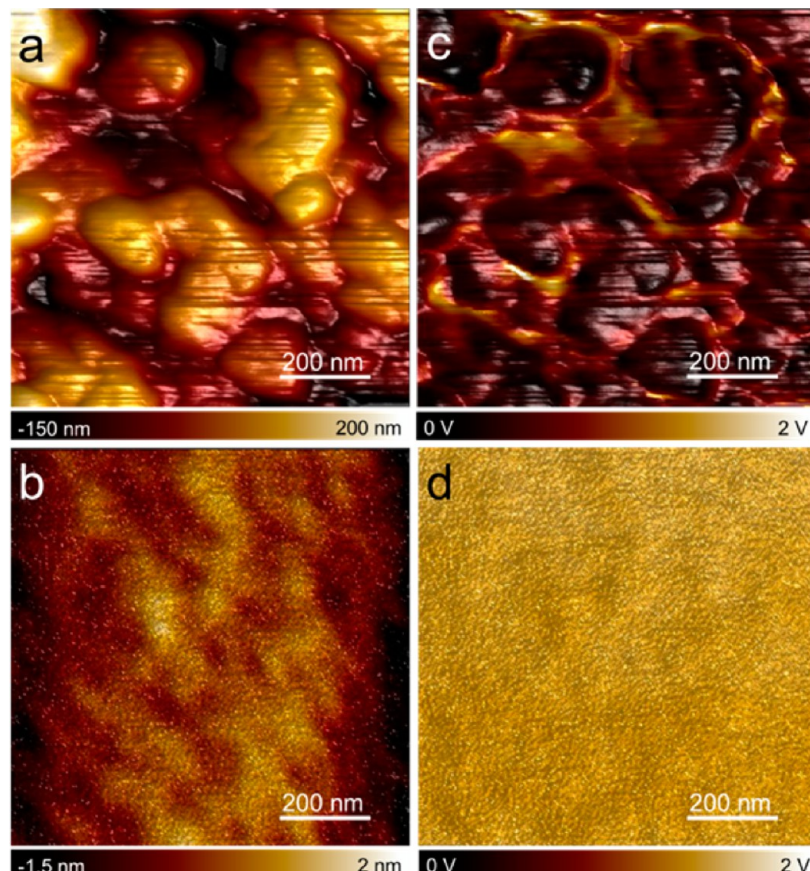
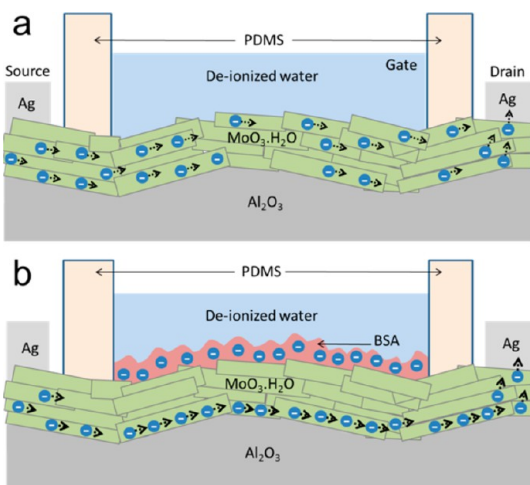


Figure 8. AFM surface roughness images of (a)  $\text{MoO}_3$  and (b) BSA on  $\text{MoO}_3$ . AFM adhesion mapping images of the (c)  $\text{MoO}_3$  and (d) BSA on  $\text{MoO}_3$  samples, for (a) and (b), respectively. The voltage scale bar directly corresponds to the adhesive force between the surface and the AFM tip.



**Figure 9.** Cross sectional schematic illustration of the  $\text{MoO}_3$  FET-based sensor (a) without BSA and (b) with BSA immobilized onto the active surface. Blue spheres indicate electrons, and the arrowheads denote their directional mobility. BSA is negatively charged.

the scanned surface. Surface adhesion for most of the  $\text{MoO}_3$  area (Figure 8c) lies below  $\sim 0.6$  V, whereas the minimum observed adhesive force for the BSA/ $\text{MoO}_3$  surface (Figure 8d) was  $> 1.3$  V. This clearly proves the dense coverage of highly adhesive BSA on the  $\text{MoO}_3$  thin film, which is in agreement with previous reports.<sup>43</sup>

On the basis of the aforesigned observations, we propose the following field effect sensing mechanism. Figure 9a illustrates the  $\text{MoO}_3$  conduction channel before BSA immobilization, and Figure 9b shows the effect of BSA on the conduction channel width. The  $\text{MoO}_3$  nanostructured thin film is composed of 2D  $\alpha\text{-MoO}_3$  nanosheets that are stacked parallel to the substrate. Collectively, these planar nanoflakes form a conduction channel with a large electron mobility that is a base for a FET of large transconductance, which results in an acceptable sensitivity. We have previously shown that the carrier mobility in individual nanoflakes with a thickness of less than 10 nm can exceed  $1100 \text{ cm}^2 \text{ V}^{-1} \text{ s}^{-1}$ .<sup>17</sup> As BSA is injected into the liquid well, it densely immobilizes onto the active surface of the  $\text{MoO}_3$  channel. The immobilization occurs in less than 10 s as the very high permittivity of  $\text{MoO}_3$  film (relative permittivity of  $\sim 300$ )<sup>45,46</sup> produces a strongly polarized surface for rapidly attracting the BSA

molecules onto the surface of the conduction channel. The negatively charged BSA produces a negative potential on the surface of the active sensing area. As the 2D  $\text{MoO}_3$  sensing film forms an n-type FET, such a negative potential results in the reduction of the channel conductance. This change in the channel conductance produces a detectable sensor response. The increase in the concentration of BSA results in more BSA molecules forming multiple layers on the active sensing surface. Such an increase in immobilized BSA molecules produces stronger electric fields, which associates with a further reduction in the channel conductance.

A discussion regarding the effect of the 2D nanostructured  $\text{MoO}_3$  film thickness on the performance of the sensors and the effect of the positive charges, in an ion-sensitive FET configuration, are presented in the Supporting Information.

## CONCLUSION

We presented a high-yield liquid phase exfoliation process to obtain a suspension solution of 2D  $\alpha\text{-MoO}_3$  nanoflakes. These nanoflakes showed to have a minimum thickness of  $\sim 1.4$  nm, corresponding to a fundamental double layer of  $\alpha\text{-MoO}_3$ . The drop-casted thin films, made of this solution, were composed of highly crystalline 2D  $\alpha\text{-MoO}_3$  nanoflakes suitable for establishing an electron conduction channel with large carrier mobility, in FET configurations. We also presented the viability of using the FET templates made of these nanostructured 2D  $\alpha\text{-MoO}_3$  films as biosensors and used BSA as a model protein to show successful biosensing behavior at different concentrations. The sensor detection limit was as small as  $250 \mu\text{g mL}^{-1}$ . The small response time (on the order of  $< 10$  s), achieved due to the high permittivity nature of the  $\text{MoO}_3$  nanoflakes, offers a highly competitive electronic-based biosensing platform.

The presented process in this paper is valuable considering the increasing interest for 2D  $\text{MoO}_3$  synthesis for electronic and optoelectronic applications. The biocompatibility of  $\text{MoO}_3$ , its high permittivity, and its large electron mobility, along with relative abundance and ease of synthesis, deem 2D  $\alpha\text{-MoO}_3$  favorable for future nanoelectronics and sensor applications.

## EXPERIMENTAL SECTION

**Exfoliation Process.** The exfoliation process of  $\text{MoO}_3$  was adopted from the report by Yao *et al.* for the exfoliation of  $\text{MoS}_2$ .<sup>34</sup> Briefly, 1 g of  $\text{MoO}_3$  nanopowder (China Rare Materials Co.) was ground for 15 min in acetonitrile (1 mL) using a mortar and pestle. The mixture was then probe sonicated (Ultrasonic Processor GEX500) for 2 h in 40 mL of an ethanol/water (1:1 ratio) solution. The resulting exfoliated  $\text{MoO}_3$  suspension was then centrifuged at 4000 rpm for 30 min in order to separate the exfoliated nanoflakes (supernatant) from the rest of the mixture.

**Device Fabrication.** The supernatant of the centrifuged suspension was drop casted on rough alumina substrates. The samples were then annealed at 220 °C for 45 min. After cooling, a 1 to 1.5 nm Au layer was deposited on the  $\text{MoO}_3$  thin films using a precision etching and coating system. This layer of Au plays two roles: (1) facilitates charge transfer from the source/drain electrodes to the film as suggested by Cattin *et al.* and Chu *et al.*,<sup>21,47</sup> as the work function of Au (5.1 eV) is aligned with the valence band of  $\text{MoO}_3$  (5.3 eV) (electrical characterization of a drop-casted 2D Au/ $\text{MoO}_3$  film can be found in the Supporting Information) and (2) provides the active surface for the model

protein in this work to be immobilized onto, as BSA has a high affinity toward gold. A cylindrical PDMS well with a volume of ~50  $\mu$ L was mechanically adhered onto the substrates covered with the thin films. Electrodes for electrical measurements were then fabricated using conductive Ag paste (Figure 2b).

**Measurements and Characterizations.** The exfoliated  $\text{MoO}_3$  suspension was characterized using UV/vis absorbance spectroscopy by means of an Ocean Optics HR4000 spectrophotometer equipped with a Micropack DH-2000 UV-vis-NIR source. TEM and HRTEM images of the  $\text{MoO}_3$  nanoflakes were acquired on a JEOL 2100F HRTEM. Cross sectional SEM images of the drop-casted thin films were obtained using an FEI Nova Nano SEM. A Bruker Multimode 8 AFM was used to analyze the surface topography as well as adhesion mapping of the  $\text{MoO}_3$  and BSA/ $\text{MoO}_3$  surfaces. XRD patterns were obtained using a Bruker D8 microdiffractometer equipped with a general area detector diffraction system. Data were collected at room temperature using a copper source with a potential of 40 kV and a current of 40 mA. A Renishaw InVia Micro-Raman system equipped with a 5 mW, 633 nm laser and a Leica microscope with a 50 $\times$  objective was used for Raman spectral analysis. A Keithley 2001 impedance analyzer with a data acquisition setup was used for attaining the dynamic sensor response.

**Conflict of Interest:** The authors declare no competing financial interest.

**Supporting Information Available:** This material is available free of charge via the Internet at <http://pubs.acs.org>.

**Acknowledgment.** S.S. and M.B. acknowledge the Australian Post-Doctoral Fellowships from the Australian Research Council through Discovery Projects DP110100262 and DP1092717, respectively. S.S. and K.K.Z. acknowledge the Australian Research Council for equipment funding through the Linkage, Infrastructure, Equipment, and Facilities Grant LE100100215. S.B. acknowledges a publication grant from the School of Graduate Research at RMIT University. The work was partially supported by the CSIRO Sensors and Sensor Networks Transformational Capability Platform (SSN TCP) and CSIRO Materials Science and Engineering Division (CMSE). The authors also would like to acknowledge the facilities and technical assistance of the Australian Microscopy & Microanalysis Research Facility at the RMIT Microscopy & Microanalysis Facility, at RMIT University.

## REFERENCES AND NOTES

1. Balendhran, S.; Walia, S.; Nili, H.; Ou, J. Z.; Zhuiykov, S.; Kaner, R. B.; Sriram, S.; Bhaskaran, M.; Kalantar-zadeh, K. Two-Dimensional Molybdenum Trioxide and Dichalcogenides. *Adv. Funct. Mater.* **2013**, *23*, 3952–3970.
2. Wang, Q. H.; Kalantar-Zadeh, K.; Kis, A.; Coleman, J. N.; Strano, M. S. Electronics and Optoelectronics of Two-Dimensional Transition Metal Dichalcogenides. *Nat. Nanotechnol.* **2012**, *7*, 699–712.
3. Late, D. J.; Liu, B.; Matte, H.; Rao, C. N. R.; Dravid, V. P. Rapid Characterization of Ultrathin Layers of Chalcogenides on  $\text{SiO}_2/\text{Si}$  Substrates. *Adv. Funct. Mater.* **2012**, *22*, 1894–1905.
4. Walia, S.; Balendhran, S.; Nili, H.; Zhuiykov, S.; Rosengarten, G.; Wang, Q. H.; Bhaskaran, M.; Sriram, S.; Strano, M. S.; Kalantar-zadeh, K. Transition Metal Oxides – Thermoelectric Properties. *Prog. Mater. Sci.* **2013**, *58*, 1443–1489.
5. Late, D. J.; Huang, Y.-K.; Liu, B.; Acharya, J.; Shirodkar, S. N.; Luo, J.; Yan, A.; Charles, D.; Waghmare, U. V.; Dravid, V. P.; et al. Sensing Behavior of Atomically Thin-Layered  $\text{MoS}_2$  Transistors. *ACS Nano* **2013**, *7*, 4879–4891.
6. Late, D. J.; Liu, B.; Matte, H. S. S. R.; Dravid, V. P.; Rao, C. N. R. Hysteresis in Single-Layer  $\text{MoS}_2$  Field Effect Transistors. *ACS Nano* **2012**, *6*, 5635–5641.
7. Radisavljevic, B.; Radenovic, A.; Brivio, J.; Giacometti, V.; Kis, A. Single-Layer  $\text{MoS}_2$  Transistors. *Nat. Nanotechnol.* **2011**, *6*, 147–150.
8. Bertolazzi, S.; Brivio, J.; Kis, A. Stretching and Breaking of Ultrathin  $\text{MoS}_2$ . *ACS Nano* **2011**, *5*, 9703–9709.
9. Radisavljevic, B.; Whitwick, M. B.; Kis, A. Integrated Circuits and Logic Operations Based on Single-Layer  $\text{MoS}_2$ . *ACS Nano* **2011**, *5*, 9934–9938.
10. Lopez-Sanchez, O.; Lemke, D.; Kayci, M.; Radenovic, A.; Kis, A. Ultrasensitive Photodetectors Based on Monolayer  $\text{MoS}_2$ . *Nat. Nanotechnol.* **2013**, *10*, 1038/nano.2013.1100.
11. Zhu, C.; Zeng, Z.; Li, H.; Li, F.; Fan, C.; Zhang, H. Single-Layer  $\text{MoS}_2$ -Based Nanoprobes for Homogeneous Detection of Biomolecules. *J. Am. Chem. Soc.* **2013**, *135*, 5998–6001.
12. Huang, K. J.; Wang, L.; Li, J.; Liu, Y. M. Electrochemical Sensing Based on Layered  $\text{MoS}_2$ -Graphene Composites. *Sens. Actuators, B* **2013**, *178*, 671–677.
13. Galatsis, K.; Li, Y. X.; Wlodarski, W.; Kalantar-zadeh, K. Sol-Gel Prepared  $\text{MoO}_3$ – $\text{WO}_3$  Thin-Films for  $\text{O}_2$  Gas Sensing. *Sens. Actuators, B* **2001**, *77*, 478–483.
14. Gesheva, K. A.; Ivanova, T. M.; Bodurov, G. Transition Metal Oxide Films: Technology and “Smart Windows” Electrochromic Device Performance. *Prog. Org. Coat.* **2012**, *74*, 635–639.
15. Lu, J. P.; Sun, C.; Zheng, M. R.; Wang, Y. H.; Nripan, M.; van Kan, J. A.; Mhaisalkar, S. G.; Sow, C. H. Ultrasensitive Phototransistor Based on K-Enriched  $\text{MoO}_3$  Single Nanowires. *J. Phys. Chem. C* **2012**, *116*, 22015–22020.
16. Rahmani, M. B.; Keshmiri, S. H.; Yu, J.; Sadek, A. Z.; Al-Mashat, L.; Moafi, A.; Latham, K.; Li, Y. X.; Wlodarski, W.; Kalantar-zadeh, K. Gas Sensing Properties of Thermally Evaporated Lamellar  $\text{MoO}_3$ . *Sens. Actuators, B* **2010**, *145*, 13–19.
17. Balendhran, S.; Deng, J. K.; Ou, J. Z.; Walia, S.; Scott, J.; Tang, J. S.; Wang, K. L.; Field, M. R.; Russo, S.; Zhuiykov, S.; et al. Enhanced Charge Carrier Mobility in Two-Dimensional High Dielectric Molybdenum Oxide. *Adv. Mater.* **2013**, *25*, 109–114.
18. Kalantar-zadeh, K.; Tang, J.; Wang, M.; Wang, K. L.; Shailos, A.; Galatsis, K.; Kojima, R.; Strong, V.; Lech, A.; Wlodarski, W.; et al. Synthesis of Nanometre-Thick  $\text{MoO}_3$  Sheets. *Nanoscale* **2010**, *2*, 429–433.
19. Meyer, J.; Hamwi, S.; Kroger, M.; Kowalsky, W.; Riedl, T.; Kahn, A. Transition Metal Oxides for Organic Electronics: Energetics, Device Physics and Applications. *Adv. Mater.* **2012**, *24*, 5408–5427.
20. Zhao, D. W.; Sun, X. W.; Jiang, C. Y.; Kyaw, A. K. K.; Lo, G. Q.; Kwong, D. L. Efficient Tandem Organic Solar Cells with an  $\text{Al}/\text{MoO}_3$  Intermediate Layer. *Appl. Phys. Lett.* **2008**, *93*, 083305.
21. Cattin, L.; Dahou, F.; Lare, Y.; Morsli, M.; Tricot, R.; Houari, S.; Mokrani, A.; Jondo, K.; Khelil, A.; Napo, K.; et al.  $\text{MoO}_3$  Surface Passivation of the Transparent Anode in Organic Solar Cells Using Ultrathin Films. *J. Appl. Phys.* **2009**, *105*, 034507.
22. Hancox, I.; Chauhan, K. V.; Sullivan, P.; Hatton, R. A.; Moshar, A.; Mulcahy, C. P. A.; Jones, T. S. Increased Efficiency of Small Molecule Photovoltaic Cells by Insertion of a  $\text{MoO}_3$  Hole-Extracting Layer. *Energy Environ. Sci.* **2010**, *3*, 107–110.
23. Brown, P. R.; Lunt, R. R.; Zhao, N.; Osedach, T. P.; Wanger, D. D.; Chang, L. Y.; Bawendi, M. G.; Bulovic, V. Improved Current Extraction from  $\text{ZnO}/\text{PbS}$  Quantum Dot Heterojunction Photovoltaics Using a  $\text{MoO}_3$  Interfacial Layer. *Nano Lett.* **2011**, *11*, 2955–2961.
24. Sreedhara, M. B.; Matte, H. S. S. R.; Govindaraj, A.; Rao, C. N. R. Synthesis, Characterization, and Properties of Few-Layer  $\text{MoO}_3$ . *Chem.—Asian J.* **2013**, *10*, 1002/asia.201300470.
25. Ando, T.; Fowler, A. B.; Stern, F. Electronic Properties of Two-Dimensional Systems. *Rev. Mod. Phys.* **1982**, *54*, 437–672.
26. Sze, S. M.; Ng, K. K. *Physics of Semiconductor Devices*, 3rd ed.; John Wiley & Sons Ltd.: New York, 2006.
27. Zheng, G. F.; Patolsky, F.; Cui, Y.; Wang, W. U.; Lieber, C. M. Multiplexed Electrical Detection of Cancer Markers with Nanowire Sensor Arrays. *Nat. Biotechnol.* **2005**, *23*, 1294–1301.
28. Medintz, I. L.; Uyeda, H. T.; Goldman, E. R.; Mattoussi, H. Quantum Dot Bioconjugates for Imaging, Labelling and Sensing. *Nat. Mater.* **2005**, *4*, 435–446.

29. Bouzidi, A.; Benramdane, N.; Tabet-Derranz, H.; Mathieu, C.; Khelifa, B.; Desfeux, R. Effect of Substrate Temperature on The Structural and Optical Properties of  $\text{MoO}_3$  Thin Films Prepared by Spray Pyrolysis Technique. *Mater. Sci. Eng., B* **2003**, *97*, 5–8.

30. Ou, J. Z.; Campbell, J. L.; Yao, D.; Wlodarski, W.; Kalantar-zadeh, K. In-Situ Raman Spectroscopy of  $\text{H}_2$  Gas Interaction with Layered  $\text{MoO}_3$ . *J. Phys. Chem. C* **2011**, *115*, 10757–10763.

31. Coleman, J. N.; Lotya, M.; O'Neill, A.; Bergin, S. D.; King, P. J.; Khan, U.; Young, K.; Gaucher, A.; De, S.; Smith, R. J.; et al. Two-Dimensional Nanosheets Produced by Liquid Exfoliation of Layered Materials. *Science* **2011**, *331*, 568–571.

32. Cunningham, G.; Lotya, M.; Cucinotta, C. S.; Sanvito, S.; Bergin, S. D.; Menzel, R.; Shaffer, M. S. P.; Coleman, J. N. Solvent Exfoliation of Transition Metal Dichalcogenides: Dispersibility of Exfoliated Nanosheets Varies Only Weakly between Compounds. *ACS Nano* **2012**, *6*, 3468–3480.

33. Smith, R. J.; King, P. J.; Lotya, M.; Wirtz, C.; Khan, U.; De, S.; O'Neill, A.; Duesberg, G. S.; Grunlan, J. C.; Moriarty, G.; et al. Large-Scale Exfoliation of Inorganic Layered Compounds in Aqueous Surfactant Solutions. *Adv. Mater.* **2011**, *23*, 3944–3948.

34. Yao, Y.; Tolentino, L.; Yang, Z.; Song, X.; Zhang, W.; Chen, Y.; Wong, C.-p. High-Concentration Aqueous Dispersions of  $\text{MoS}_2$ . *Adv. Funct. Mater.* **2013**, *10.1002/adfm.201201843*.

35. Garcia, P. F.; McCarron, E. M. Synthesis and Properties of Thin Film Polymorphs of Molybdenum Trioxide. *Thin Solid Films* **1987**, *155*, 53–63.

36. Leung, A.; Shankar, P. M.; Mutharasan, R. Real-Time Monitoring of Bovine Serum Albumin at Femtogram/ml Levels on Antibody-Immobilized Tapered Fibers. *Sens. Actuators, B* **2007**, *123*, 888–895.

37. Liu, R. T.; Yang, J. H.; Sun, C. X.; Wu, X.; Li, L.; Li, Z. M. Resonance Light-Scattering Method for the Determination of BSA and HSA with Sodium Dodecyl Benzene Sulfonate or Sodium Lauryl Sulfate. *Anal. Bioanal. Chem.* **2003**, *377*, 375–379.

38. Shao, M.; Lu, L.; Wang, H.; Luo, S.; Ma, D. Microfabrication of a New Sensor Based on Silver and Silicon Nanomaterials, and its Application to the Enrichment and Detection of Bovine Serum Albumin via Surface-Enhanced Raman Scattering. *Microchim. Acta* **2009**, *164*, 157–160.

39. Xu, X.; Huang, J.; Li, J.; Yan, J.; Qin, J.; Li, Z. A Graphene Oxide-Based AIE Biosensor with High Selectivity towards Bovine Serum Albumin. *Chem. Commun.* **2011**, *47*, 12385–12387.

40. Chen, H. J.; Zhang, Z. H.; Xie, D.; Cai, R.; Chen, X.; Liu, Y. N.; Yao, S. Z. Surface-Imprinting Sensor Based on Carbon Nanotubes/Graphene Composite for Determination of Bovine Serum Albumin. *Electroanalysis* **2012**, *24*, 2109–2116.

41. Shao, M.-W.; Yao, H.; Zhang, M.-L.; Wong, N.-B.; Shan, Y.-Y.; Lee, S.-T. Fabrication and Application of Long Strands of Silicon Nanowires as Sensors for Bovine Serum Albumin Detection. *Appl. Phys. Lett.* **2005**, *87*, 183106.

42. Siciliano, T.; Tepore, A.; Filippo, E.; Micocci, G.; Tepore, M. Characteristics of Molybdenum Trioxide Nanobelts Prepared by Thermal Evaporation Technique. *Mater. Chem. Phys.* **2009**, *114*, 687–691.

43. Silva-Bermudez, P.; Rodil, S. E.; Muhl, S. Albumin Adsorption on Oxide Thin Films Studied by Spectroscopic Ellipsometry. *Appl. Surf. Sci.* **2011**, *258*, 1711–1718.

44. Song, L.; Yang, K.; Jiang, W.; Du, P.; Xing, B. S. Adsorption of Bovine Serum Albumin on Nano and Bulk Oxide Particles in Deionized Water. *Colloids Surf., B* **2012**, *94*, 341–346.

45. Naouel, R.; Dhaouadi, H.; Touati, F.; Gharbi, N. Synthesis and Electrical Properties of Well-Ordered Layered  $\text{Alph}-\text{MoO}_3$  Nanosheets. *Nano-Micro Lett.* **2011**, *3*, 242–248.

46. Saad, E. Dielectric Properties of Molybdenum Oxide Thin Films. *J. Optoelectron. Adv. Mater.* **2005**, *7*, 2743–2752.

47. Chu, C. W.; Li, S. H.; Chen, C. W.; Shrotriya, V.; Yang, Y. High-Performance Organic Thin-Film Transistors with Metal Oxide/Metal Bilayer Electrode. *Appl. Phys. Lett.* **2005**, *87*, 193508.